



Changes in microstructure and properties of weld heat-affected zone of high-strength low-alloy steel

Shu-jun Jia¹ · Qi-lin Ma^{1,2} · Yu Hou³ · Ba Li¹ · He-song Zhang¹ · Qing-you Liu¹

Received: 29 July 2023 / Revised: 23 August 2023 / Accepted: 23 August 2023 / Published online: 2 January 2024
© China Iron and Steel Research Institute Group Co., Ltd. 2024

Abstract

The evolution of the microstructure and toughness of APL5L X80 pipeline steel after thermal welding simulation was investigated by X-ray diffraction, electron backscatter diffraction, and transmission electron microscopy. The results indicated that primary heat-affected zones can be divided into weld, coarse-grained, fine-grained, intercritical, and subcritical zones. The microstructure of the weld zone is mainly composed of bainitic ferrite and a small amount of granular bainite; however, the original austenite grains are distributed in the columnar grains. The structure of the coarse-grained zone is similar to that of the weld zone, but the original austenite grains are equiaxed. In contrast, the microstructure in the fine-grained zone is dominated by fine granular bainite, and the effective grain size is only 8.15 μm , thus providing the highest toughness in the entire heat-affected zone. The intercritical and subcritical zones were brittle valley regions, and the microstructure was dominated by granular bainite. However, the martensite–austenite (M/A) constituents are present in island chains along the grain boundaries, and the coarse size of the M/A constituents seriously reduces the toughness. The results of the crack propagation analyzes revealed that high-angle grain boundaries can significantly slow down crack growth and change the crack direction, thereby increasing the material toughness. The impact toughness of the low-temperature tempering zone was equivalent to that of the columnar grain zone, and the impact toughness was between those of the critical and fine-grained zones.

Keywords Welding thermal simulation · Impact toughness · Crack propagation · Martensite–austenite constituent · High-strength low-alloy steel weld · Heat-affected zone

1 Introduction

Since the 1990s, the use of high-strength low-alloy (HSLA) steel in the oil and gas industry has grown rapidly [1–3], and the steel used in pipelines has changed from the first-generation X52, X60, and X65 alloys to current high-grade steel alloys, represented by X80, X100, and X120 [4–6]. As

a result of the long length of pipelines, segments must be jointed by welding. However, the composition and structure of welded joints are not homogeneous, and faults impair and weaken their performance [7–11]. A final-failure study of several pipeline incidents revealed that the quality issues of welded joint were responsible [12–15], and the performance analysis of welded joints is a popular topic in the field of pipeline steel research [16–20]. In general, welded-joint structures can be divided into weld seams and heat-affected zones. Cladding is frequently used along with the base metal to create weld-seam structures, and the produced seam has a higher strength than the base metal [21, 22]. During welding, the affected area is exposed to a range of temperatures and, thus, often exhibits a range of microstructural states. The presence of these microstructures makes the material more susceptible to stress concentration, which can result in cracking under stress [23]. Furthermore, the welding process frequently

✉ Shu-jun Jia
jjajsj504@126.com

¹ Central Iron and Steel Research Institute Co., Ltd.,
Beijing 100081, China

² Collaborative Innovation Center for Steel Commonality,
University of Science and Technology Beijing,
Beijing 100083, China

³ Construction Project Management Branch of China National
Petroleum Pipeline Network Group Co., Ltd.,
Langfang 065000, Hebei, China

involves multiple passes and layers that repeatedly affect the matching structure. Therefore, the structure and function of welded junctions require further study.

Many researchers have conducted studies of needle welded joints. For example, Arora et al. [24] used thermal simulations to simulate the toughness of X80 pipeline steel at 1050 °C, but when the second peak temperature was in the intercritical zone (800 °C), many martensite–austenite (M/A) constituents appeared at the grain boundaries of the experimental steel, and the impact toughness was significantly reduced. Thus, they identified the causes of the significant decrease in the toughness of the secondary critical region and offered a plausible explanation for it. However, their study primarily focused on the major coarse-grained secondary critical regions in the heat-affected zone, but concerning the entire welded joint, the weak points are not isolated to the secondary critical area. Therefore, further work is needed. Jorge et al. [25] summarized the relationship between the composition of pipeline steel and the toughness of various microstructures after thermal simulation. High-niobium steel was found to have the lowest impact energy in the coarse-grained area, and a significant number of martensitic structures were evident in its corresponding microstructure, demonstrating that the formation of M/A constituents must be controlled by designing an appropriate chemical composition to reduce the equivalent carbon and welding coefficient. However, to date, the weld heat-affected zone has only been studied in a few specific locations.

Yang et al. [26] quantified the microstructure of a simulated coarse-grained heat-affected zone (CGHAZ) with a heat input of 10–100 kJ/cm to determine the relationship between the welding heat input of HSLA steel and the fracture toughness of the CGHAZ. It was discovered that the crack tip opening displacement (CTOD) at – 20 °C decreased with the increase in heat input, and the reason for this was that the increase in heat input caused the bainite transition temperature and conversion time to increase. This resulted in the formation of a large concentration of granular bainite (GB) and M/A constituents, which lowers the low-temperature toughness of the material. Ramirez et al. [27] investigated the microstructure of X80 pipeline steel and its homogeneity at different cooling rates. Samples with inclusions and segregation bands had low hydrogen-induced cracking (HIC) resistance, whereas samples with only ferrite and GB and no segregation bands had much higher HIC resistance. It has also been found that the presence of a medium-angle boundary prevents the development of microcracks and the spread of fractures in the microstructure. To date, such studies have focused on the HIC of the microstructure at different cooling rates and found that inclusions and segregation regions seriously affect the hydrogen embrittlement resistance of materials;

however, further verification and research into the overall weld toughness, which have a significant impact on the material, are required. Huda et al. [28] used two different cooling rates in heating simulations and found that the size, distribution, and morphology of the M/A constituents changed, but the M/A constituent content remained comparable. Furthermore, the M/A constituents formed at 2 °C/s were coarse, and the coarse M/A constituent were surrounded by ferrite grains, showing a higher local grain dislocation. Consequently, there is a large amount of inhomogeneous deformation and dislocation activity, which accelerates the development of voids. The studies described above focused on material toughness and provided additional detailed characterization, but did not establish a link between the intact heat-affected zone and the properties or microstructure.

Because welded joints often fail, the study of the structural factors that contribute to such failure has been a long-standing topic of controversy in pipeline steel research. Although considerable research has been conducted in this area, most studies have focused on a single temperature range, there is a lack of understanding how the entire welded-joint structure changes over time. Furthermore, the repeated thermal cycling in actual welded structures makes it impossible for two simple thermal simulations to explain the microstructure fully. Therefore, in this study, thermal simulation technology was used to characterize the microstructure of each region of the X80 pipeline steel accurately and understand the relationship between structure and performance.

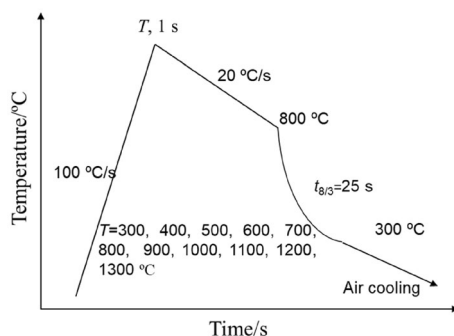
2 Materials and methods

The composition of the test steel, which was smelted in a 200-kg vacuum induction furnace in the laboratory, is presented in Table 1. High-purity iron was used as the primary raw material for smelting to minimize the negative effects of S, P, O, N, and other impurity elements on the toughness. After smelting, the ingots were formed into rough square blanks with a cross-section of 100 mm × 80 mm cross-section, and the rough billets were divided, heated to 1200 °C in a heating furnace, held for 30 min, and then rolled into steel plates with a thickness of 18.4 mm on an experimental rolling mill. The impact samples with size of 10 mm × 10 mm × 55 mm were horizontally cut and processed from the base metal and the welding heat simulation sample, respectively, and impact test was carried out at – 10 °C on the JBN-300N testing machine according to the standard GB/T 229—2020. The tensile test was performed according to the standard GB/T 228.3—2019. The tensile properties of longitudinal samples were measured using an Instron-5958 electronic universal testing

Table 1 Chemical composition of test steel (wt.%)

C	Si	Mn	P	S	Cr	Ni	Mo	Cu	Nb	V	Ti	Fe
0.05	0.2	1.5	0.009	≤ 0.001	0.29	0.1	0.2	0.1	0.05	0.03	0.01	Balance

machine at tensile strain rate of $1 \times 10^{-3} \text{ s}^{-1}$ and loading rate of 1 mm/min. After electrical discharge machining (EDM) to shape the steel plate into squares of 11 mm × 11 mm × 80 mm, a Gleeble-3800 thermal–mechanical physical simulation system was employed to simulate the self-protection flux cored welding of X80 pipe during the welding process (Fig. 1). In the welding heat simulation experiments, each piece was polished using 150–1000 grit sandpaper before being transferred to a polishing machine for blow drying and polishing. The surface of the sample was rinsed with water after corrosion with a 4 vol.% nitric acid alcohol solution and dried again. Subsequently, observation by scanning electron microscopy (SEM, quiten650) and elemental analysis using an integrated energy dispersive spectrometer (EDS) were carried out to characterize the microstructural evolution of the test steel. Electron backscatter diffraction (EBSD) was conducted using an accelerating voltage of 10 kV, a scanning area of $100 \mu\text{m} \times 100 \mu\text{m}$, and 0.25- μm steps (Oxford Nordlys F +). The sample were mechanically ground, polished, and electrolytically polished in 10 vol.% perchlorate alcohol [29, 30]. Three SEM images from various fields of view were used to calculate the effective grain size (high-angle grain boundary > 15°) [31–33]. The microstructure, precipitation, and dislocations of the materials were all examined by transmission electron microscopy (TEM, Tecnai G2 F20). The sample for TEM was produced with a thickness of less than 5 mm, formed into a thin sheet with a diameter of 3 mm, and then treated with a 10 vol.% perchloric acid and 90 vol.% alcohol solution for double spray polishing, with the double spray parameters of 50–80 mA and 20 °C [34, 35].

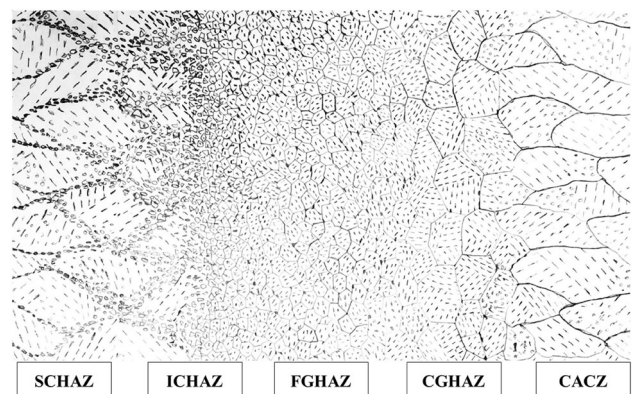
**Fig. 1** Thermal simulation process. T —Temperature; $t_{8/5}$ —time needed for temperature drop from 800 to 300 °C

3 Results and discussion

3.1 Weld microstructure

Figure 2 shows a schematic of the microstructure of each area in the heat-affected zone of X80 self-shielding ring welding. From left to right, the subcritical heat-affected zone (SCHAZ), intercritical heat-affected zone (ICHAZ), fine-grained heat-affected zone (FGHAZ), CGHAZ, and columnar austenite crystal zone (CACZ) are shown. Based on the analysis of the microstructural characteristics of each area of the heat-affected zone under a single heating cycle, the entire width of the weld was analyzed. The SCHAZ, ICHAZ, FGHAZ, CGHAZ, and CACZ correspond to 500, 800, 900, 1100, and 1300 °C, respectively.

The detection area undergoes welding thermal cycles, and the initial primary dendrite structure austenitizes at high temperatures (i.e., above 1300 °C) and transforms into coarse equiaxed austenite. Figure 3a, b illustrates the CACZ structure of the simulated weld, having maximum and average widths of more than 100 μm and approximately 70 μm , respectively. Figure 3c, d presents the microstructure of the CGHAZ, which consists mainly of M/A constituents and coarse GB. The volume fraction of M/A constituents in the coarse-grained region ranges from 20% to 40%, having a typical morphology of large square or circular shapes, with many irregular sharp angles and a coarse particle size distribution, and having an average diameter between 2 and 5 μm . The statistical information was obtained using ImageJ analysis of the M/A constituents from three different fields of view.

**Fig. 2** Schematic of microstructure of heat-affected zone of weld

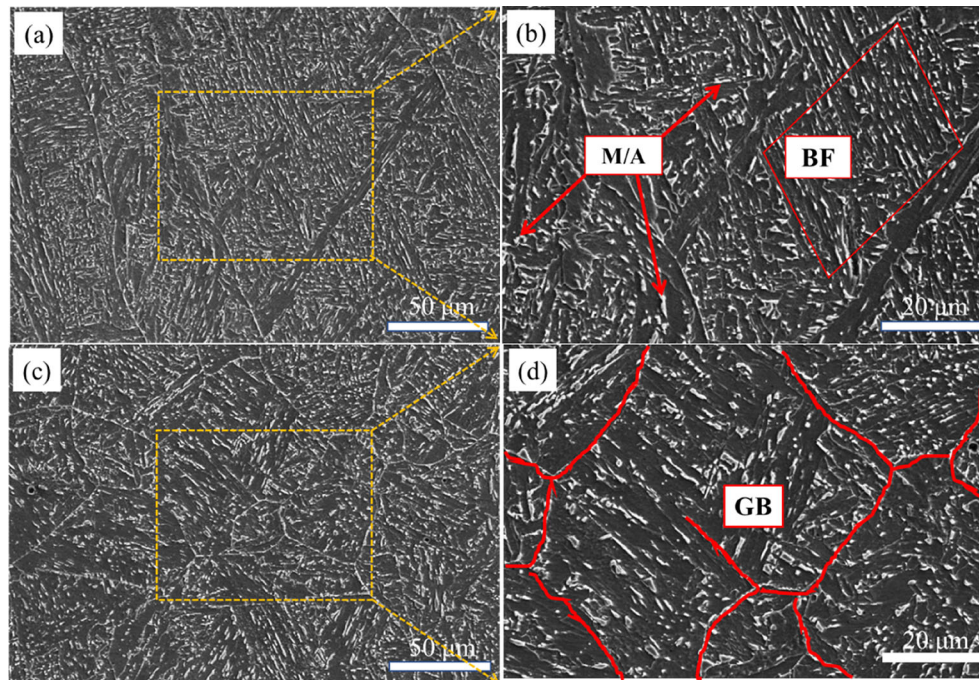


Fig. 3 SEM structure of CACZ (a, b) and CGHAZ (c, d). BF—Bainitic ferrite

TEM images of the columnar crystals and coarse crystal areas are shown in Fig. 4. As shown in Fig. 4a, c, the bainite lath in the columnar grain region is more obvious, and the lath width is smaller, whereas the lath characteristics in the coarse-grained region are not obvious.

According to the literature [36, 37], the high martensite content in the M/A constituents of the CGHAZ and their distribution in the weak positions of the crystal are typical causes of cracks. Figure 4b illustrates the M/A typical

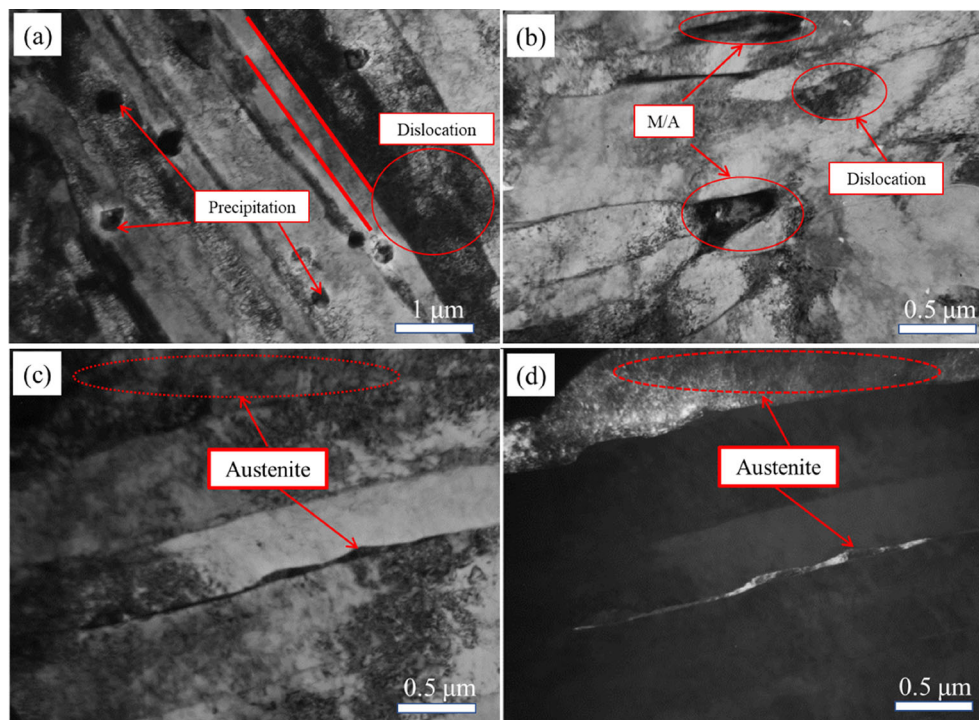


Fig. 4 TEM structure of CACZ (a, b) and CGHAZ (c, d)

distribution of M/A constituents in the shape of thick rods at the locations of the crystal bands.

The retained austenite in Fig. 4c, d is formed during rapid weld cooling. Austenite has a face-centered cubic crystal structure and excellent flexibility, and inhibits crack propagation, according to the literature [38]. Figure 4 shows that the retained austenite film distributed between the parallel laths of the bainite plate was aligned in the transmission experiments. From a crystallographic perspective, the toughness of lath bainite was higher than that of coarse GB. Crucially, as the BF structure contains many high-angle grain boundaries, it can hinder crack propagation [39, 40]. Several studies [18, 24, 38] have shown that the influence of M/A constituents on the strength and toughness of materials is related to their composition, position, size, and shape.

Compared with that of the coarse-grained area, the peak temperature of the thermal cycling process in the fine-grained area was lower, and both were higher than A_3 . However, after austenitization in the fine-grained zone, the grains became finer, and the structure obtained after the phase transformation was also finer. In the subsequent cooling process, the fine austenite grains were less stable, and the phase transformation temperature increased. Figure 5a, b shows the microstructure of the FGHAZ, which is mainly composed of GB and small M/A components. The M/A constituents content decreased, and the size was smaller than that of the M/A component in the coarse-grained region. The average volume fraction of M/A

components is in the range of 12%–25%, and the average particle size is 1–3 μm .

Based on the definition for characterizing the ICHAZ, during the welding heat cycle, regions with a peak temperature between A_1 and A_3 undergo partial austenitization. When the alloying elements in the austenite are high, the austenite is stable, and the phase transformation temperature in the subsequent cooling process is low, forming martensite or room-temperature-retained austenite to form M/A islands. The amount of austenitization increased with the increase in the peak temperature of the thermal cycle, and austenitization only occurred near the grain boundaries in the temperature region close to A_1 .

Therefore, the microstructural distribution of the two-phase zone in the heat-affected zone of the weld was generally uneven, and many hard-phase M/A islands were either clustered or formed island chains. Figure 5c, d shows the microstructure of the ICHAZ, where the matrix structure is GB and contains many large-sized M/A components. Based on the statistics, the M/A component volume fraction in the two-phase region can reach about 30% on average, and the particle size, especially the maximum size of the M/A island chain, can reach approximately 5–8 μm .

Figure 6a, b shows the TEM images of the microstructure of the fine-grained region and the lath and massive ferrite structures in the GB. The massive ferrite has a low dislocation density, an average diameter of about 2 μm , and a lath width of between 800 and 1300 nm. Compared to the lath bainite, which has a higher dislocation density,

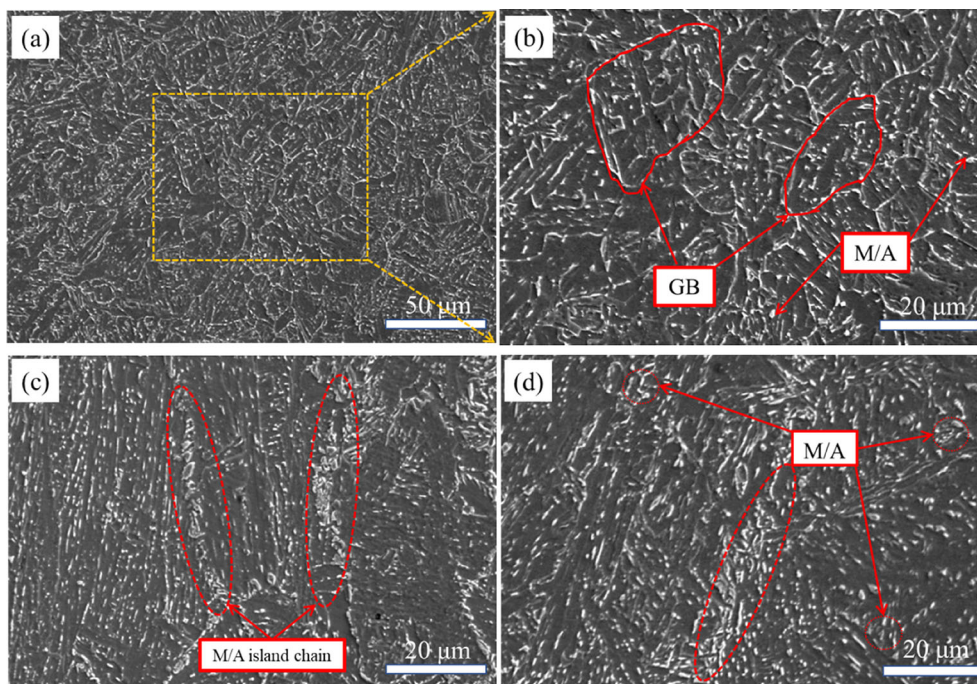


Fig. 5 SEM images of FGHAZ (a, b) and ICHAZ (c, d)

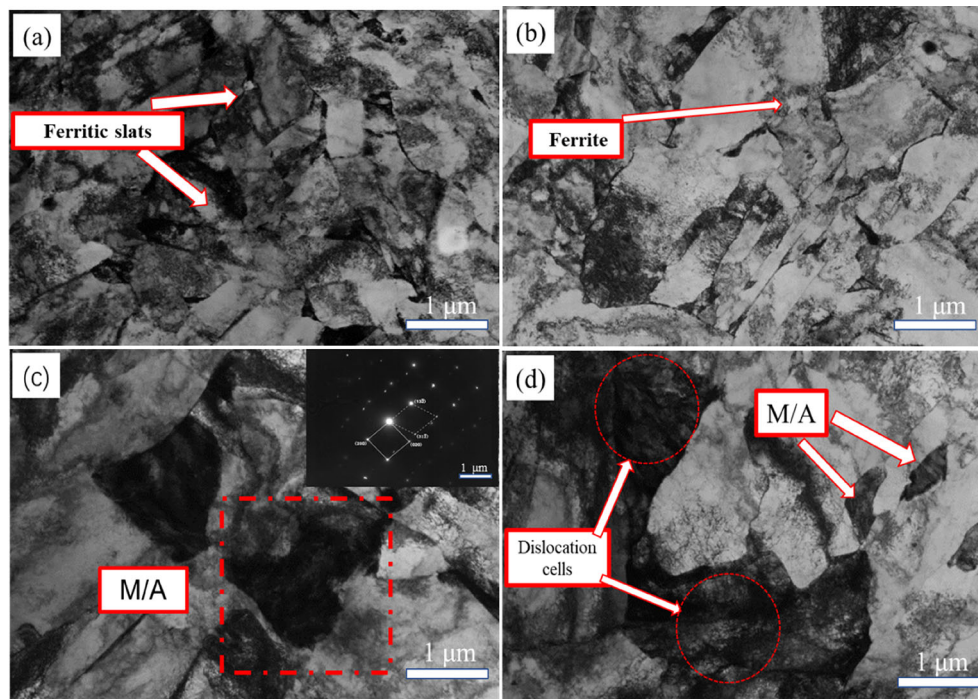


Fig. 6 TEM images of FGHAZ (a, b) and ICHAZ (c, d)

the large ferrite particles have a relatively low dislocation density. The microstructure also contains a small amount of fine massive M/A constituents with a length of about 1 μm . Figure 6c, d shows the TEM images of the microstructure in the intercritical region, where a large number of rod-shaped and layered M/A islands are distributed in the ferrite matrix. As shown in Fig. 6c, there are darker M/A islands at the grain boundaries of the lath and block structures, and the M/A constituent also mainly exists in the form of blocks. Electron diffraction measurements further confirmed the M/A constituent. Most of the M/A constituents are located at the grain boundaries (i.e., the interface between the lath structure and the block structure) and the edge of the massive ferrite. Most of these constituents are blocky, strip-like, contracted, and thick in size, and the length between islands is 2–4 μm . The lath bundle width is in the range of 0.5–1 μm , the dislocation density inside the lath is low, and the dislocations are mainly entangled near the M/A constituents.

The SCHAZ is typically the region in which the thermal simulation peak temperature is lower than that of the ICHAZ. Although there was no austenitization in this area, as the temperature increased, the substructure in the structure was further restored, the dislocation density decreased, and some of the original columnar crystal structures decomposed into long strips or islands of M/A.

Figure 7a, c shows the comparison of the SCHAZ and CACZ microstructures. Both matrix microstructures are coarse lath bainite and GB. Figure 7b, d shows a

comparison of the M/A components in the two intervals. Clearly, the size of the M/A island in the CACZ is significantly larger than that in the SCHAZ, about 3.5 μm or even larger on average. However, the M/A components in the SCHAZ tended to exhibit an island or rod shape, a smaller size, and a significantly more dispersed visible distribution. Some M/A components are distributed as long rods. As mentioned, it has been reported that the M/A component morphology has a significant impact on the toughness of the matrix, especially for long rod and lath M/A components with low toughness [40].

3.2 Impact toughness in heat-affected zone

Figure 8a presents the impact load–displacement curves at different peak temperatures. The load–displacement curve shows that the load of more than 3000 N is required to cause cracks at peak temperatures of 1300, 1100, and 200 $^{\circ}\text{C}$, indicating the high stress resistance of the material. However, the load drops to around 2000 N at peak temperatures of 800 or 500 $^{\circ}\text{C}$, implying that the material is more prone to cracking at low stress. After reaching the maximum load, the cracks start to propagate. The curves at 800 and 500 $^{\circ}\text{C}$ show a rapid decline after the maximum load, suggesting that the crack growth is unstable and catastrophic. In contrast, the curves at 1300, 1100, and 200 $^{\circ}\text{C}$ show a gradual decrease after a short plateau, indicating that the crack growth is stable and controlled. The area between the load–displacement curve and the

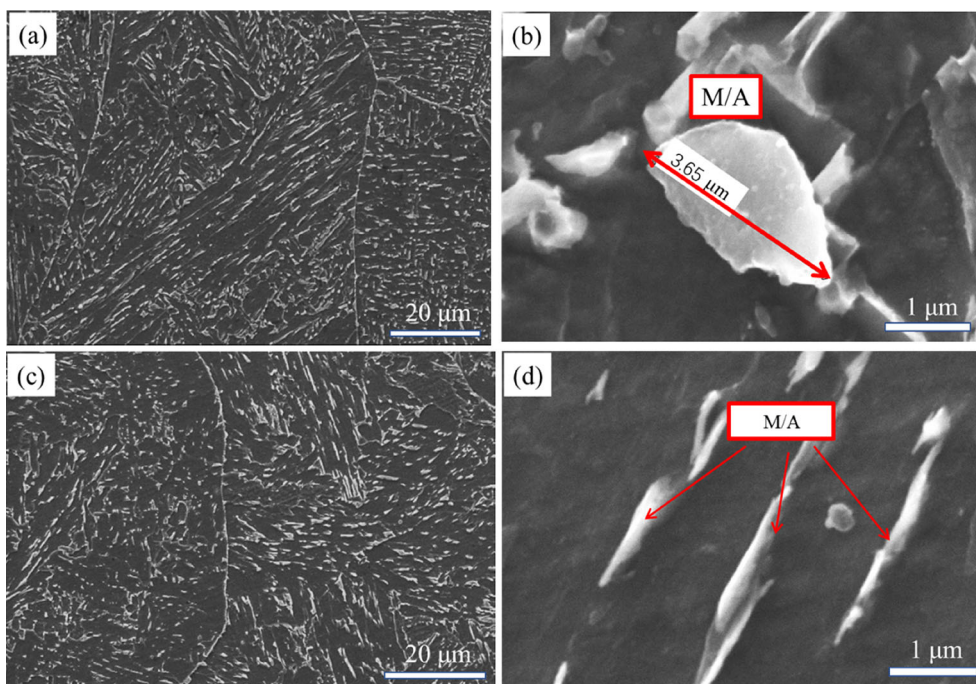


Fig. 7 Comparison of microstructure and M/A in CACZ (a, b) and SCHAZ (c, d)

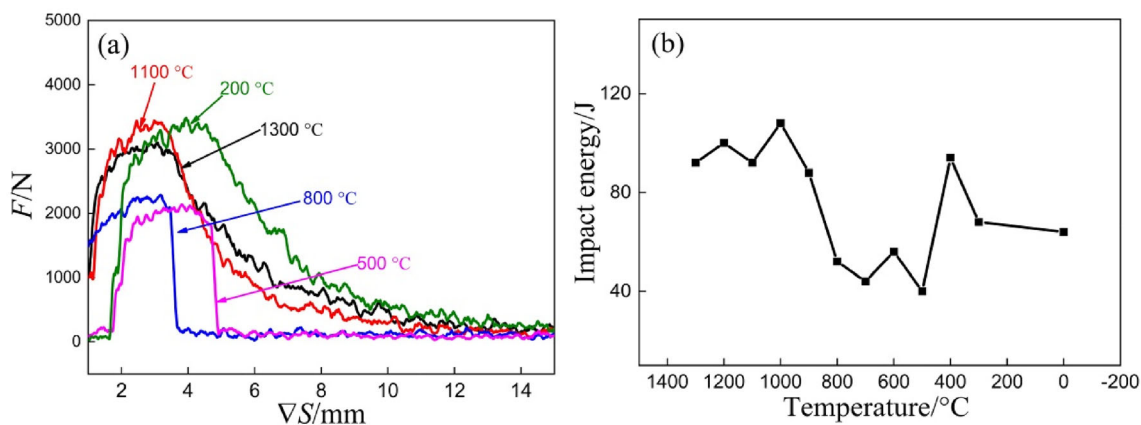


Fig. 8 Shock load–displacement curves at several typical peak temperatures. **a** Stress–strain curve; **b** impact work curve. *F*—Impact force; ∇S —crack tip displacement

horizontal axis represents the work done by the material [41]. Figure 8b displays the impact toughness tests at different peak temperatures. The impact toughness varies significantly across the experimental temperature range, which can be roughly divided into three regions according to the toughness level. When the peak temperature is above 900 °C, the region has the highest toughness level, where the impact energy at $-10\text{ }^{\circ}\text{C}$ is greater than 90 J. When the peak temperature is below 400 °C, the region has the intermediate toughness level, where the impact energy is between 40 and 60 J. When the peak temperature is between 800 and 500 °C, the region has the lowest

toughness level, where the impact energy is about 45 J, and it corresponds to the brittle zone of the material.

3.3 Microstructure and fracture toughness

The size and angle grain-boundary diagrams for the CACZ and CGHAZ are shown in Fig. 9, where the thick black line denotes the high-angle grain boundary with an orientation difference greater than 15° , and the thin red line denotes the low-angle grain boundary with an orientation difference of 2° to 15° . The microstructure of the CGHAZ is depicted in Fig. 9c, d, in which the austenite grain size is

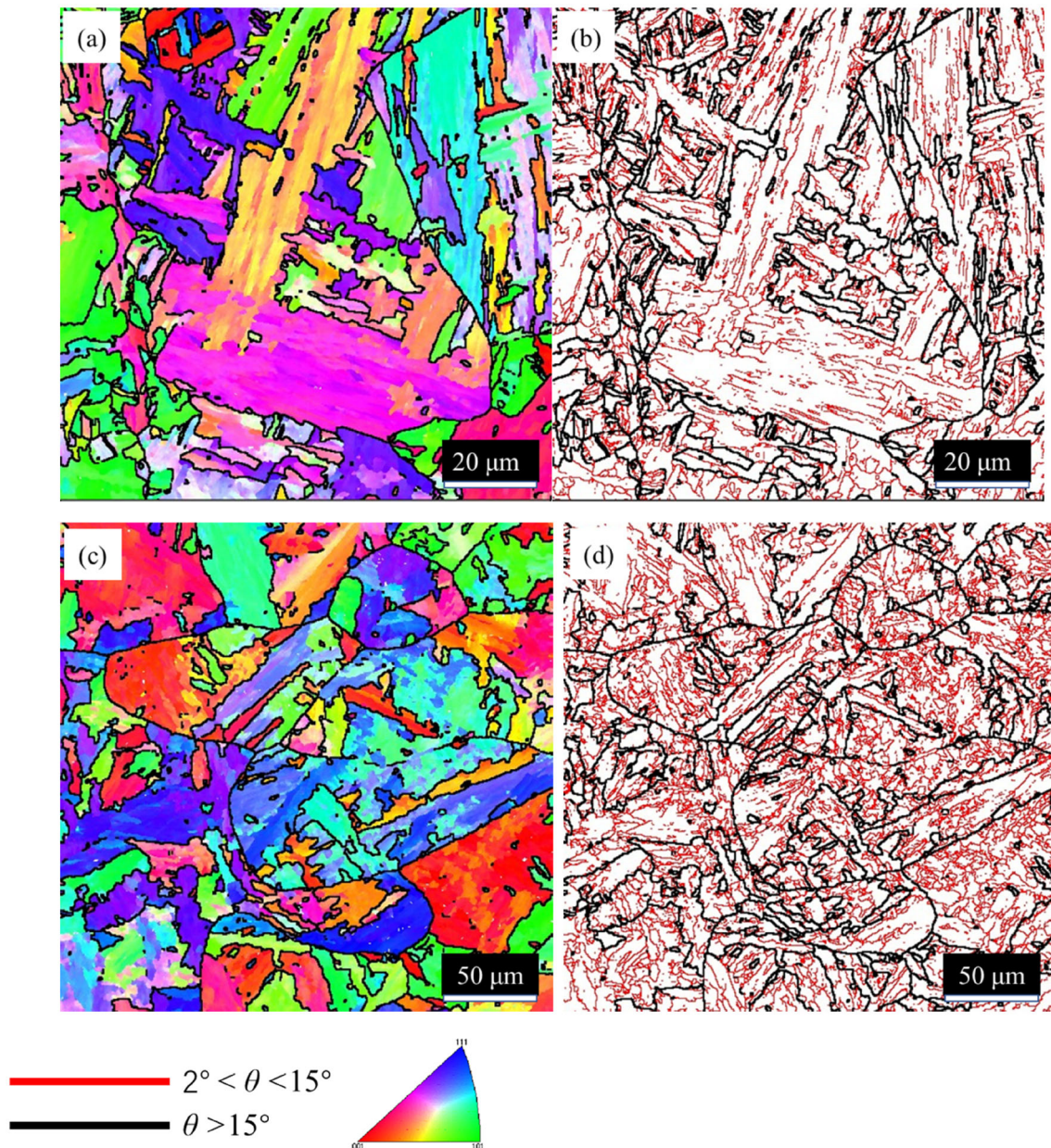


Fig. 9 Microstructure of CACZ (**a**, **b**) and CGHAZ (**c**, **d**) by EBSD. θ —Grain boundary misorientation

noticeably smaller than that of the columnar crystals, and the number of MAs in the tissue is noticeably higher.

Figure 9 illustrates the use of EBSD to observe high-angle grain boundaries in the coarse-grained region. This reveals that the original austenite grain boundary is a typical high-angle grain boundary that matches the morphology observed through SEM. Additionally, the austenite grains contained numerous slats and slab blocks. This is because the lattice constant increased and the volume expanded as the supercooled austenite transformed into martensite. Consequently, elastic distortion energy accumulated during the phase transition process. There are

multiple slats and plates with different orientations within a single grain, and the boundaries of the slat bundles and plates are high-angle grain boundaries. This is because, when the elastic distortion energy builds up to a certain point, it is frequently released through its own coordination mechanism.

The inverse pole figure (IPF) and high- and low-angle grain boundary diagrams of the FGHAZ and ICHAZ were obtained using EBSD, and the results are presented in Fig. 10. Comparing the two zones, the structures in the FGHAZ are smaller, and the density of high-angle grain boundaries in the structure increases. In contrast, there are

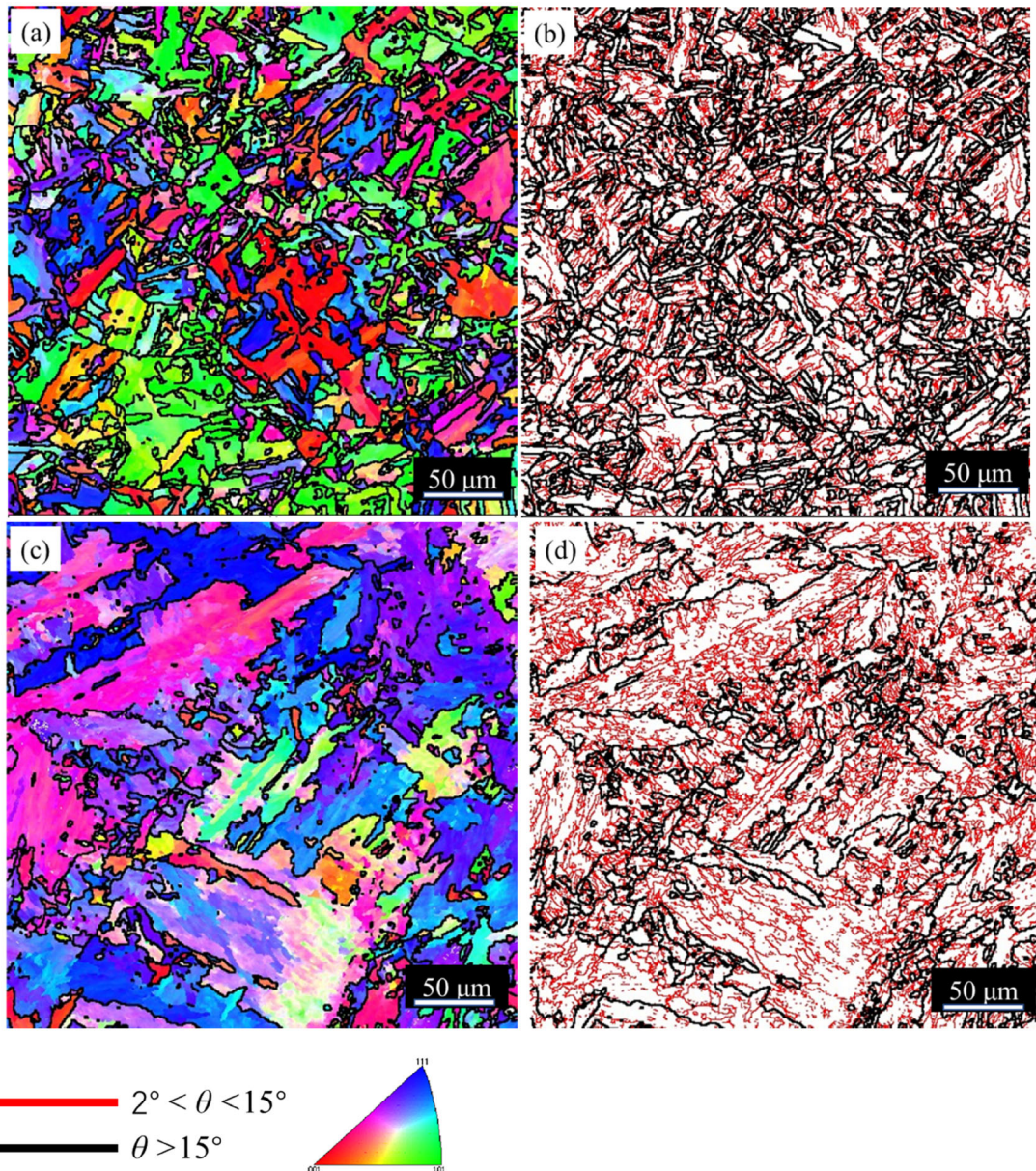


Fig. 10 Microstructure of FGHAZ (a, b) and ICHAZ (c, d) by EBSD

small islands of local agglomeration in the ICHAZ structure, but the overall structural state is relatively coarse, the density of low-angle grain boundaries is high, and there are relatively few high-angle grain boundaries. Using the Channel-5 program to count the effective grain size, the average effective grain size of the FGHAZ was found to be the smallest, only 8.15 μm . In the two-phase region, the effective grain size of ICHAZ was still 19.6 μm because of the large degree of agglomeration of M/A components from the crystallographic point of view.

Figure 10 illustrates the characteristics of the ICHAZ size and angle grain boundaries. Clearly, the density of the high-angle grain boundary is higher in the region where the

M/A components are concentrated close to the original austenite grain boundary because the M/A component boundary is also a high-angle grain boundary. As a result, the high-angle grain boundary in this region is primarily a closed small circle, indicating that the M/A component accumulation in this region is the main cause of the high density of the high-angle grain boundary in this region. During thermal cycling, the original austenite that has not undergone austenitization recovers at high temperatures, and some subgrain boundaries in the crystal vanish or shrink significantly, resulting in a significant decrease in the density of grain boundaries at high angles in these areas.

The propagation process of the cracks was observed using the nickel-plating method for impact fracture, and the results are shown in Fig. 11. Figure 11a depicts the crack propagation in the CACZ interval when the direction of the crack was parallel to the direction of the columnar crystals and crack just touched the austenite grain boundary, making the crack easy to spread quickly along the austenite grain boundary, and thus greatly reducing the toughness of the material. The crack propagated in Fig. 11c is more tortuous than that in the CACZ, which has experienced multiple deflections and does not exhibit long-distance linear propagation. This indicated that cracks were more hindered when propagating in the CGHAZ, which required more energy and exhibited a higher degree of toughness.

A significant number of high- and low-angle grain boundaries caused the crack to deflect constantly when it was in the FGHAZ interval. Figure 12 illustrates the propagation condition and fracture morphological characterization of cracks in the FGHAZ and ICHAZ intervals. In addition, based on the fracture morphology, the fracture had evident dimples, and the starting locations of the ripping edges and cracks are clear. A typical cleavage fracture morphology, which is closely associated with the M/A island chain on the austenite grain boundary in the ICHAZ, was observed in the almost straight and enlarged crack propagation in the ICHAZ.

Martensite makes up a substantial portion of the M/A island in the ICHAZ. Owing to its high hardness and ease of producing stress concentrations during the deformation

process, martensite is prone to the emergence and growth of brittle cracks. Residual stress occurs around the M/A component because the martensite phase transition causes volume expansion during the generation of M/A component, and stress concentration occurs during the deformation process because M/A component is harder than the surrounding matrix. The M/A component stress fields are superimposed on one another when two or more M/A components are close to each other, thereby increasing the stress concentration. Consequently, it is simpler to initiate and spread brittle cracks when the M/A components are concentrated or dispersed close to each other, and it is more difficult to propagate cracks when they are already present. Therefore, even though the density of the high-angle grain boundary in this region is high, it frequently serves as the initiation source and propagation channel of crack in the original austenite grain boundary region, where M/A is relatively dense.

4 Conclusions

1. The microstructure of the main heat-affected zone in X80 pipeline steel was complex and diverse. The coarse-grained region had a coarse BF and GB structure. The fine-grained region had a fine GB structure. The intercritical region had island-chain-like M/A constituents at the GB grain boundaries. The subcritical region had a coarse bainite structure.

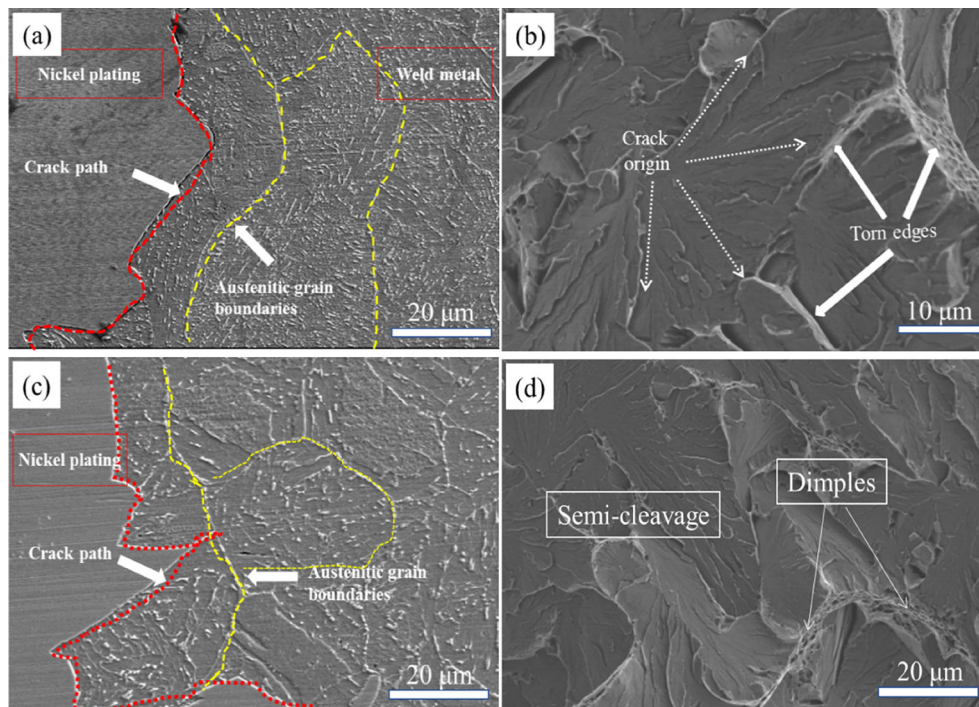


Fig. 11 Crack growth trend and fracture morphology in CACZ (a, b) and CGHAZ (c, d)

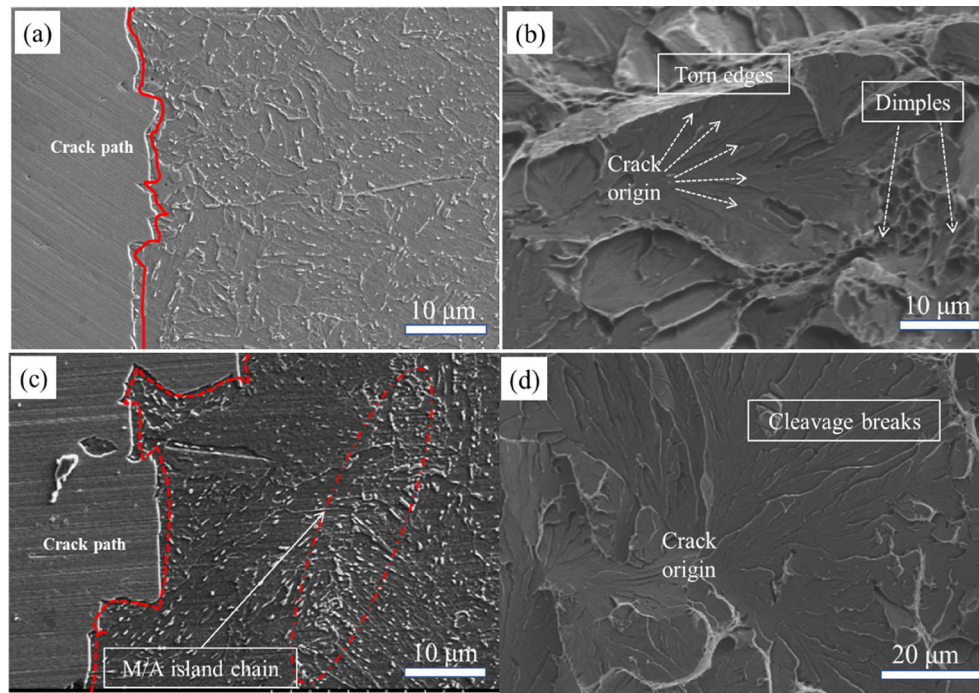


Fig. 12 Crack growth trend and fracture morphology in FGHAZ (a, b) and ICHAZ (c, d)

- The impact toughness of each part of the heat-affected zone of the weld varied significantly according to the temperature of the thermal cycle. When the thermal cycle temperature was above A_{c3} , the impact toughness of the FGHAZ increased. EBSD characterization revealed that a high density of high-angle grain boundaries in the FGHAZ was responsible for its excellent toughness. Both the ICHAZ and SCHAZ were brittle, owing to different reasons. The ICHAZ was embrittled by the coarsening and chain distribution of the M/A constituent, and its impact toughness decreased sharply. The SCHAZ was embrittled by the redistribution of the M/A constituent, which changed from an island shape to a long rod-shaped shape. Its toughness was between that of the brittle zone and the high-temperature tough zone, which was similar to the columnar-grain zone.
- By examining the relationship between the fracture toughness and microstructural characteristics in each region, we found that the high-angle grain boundary density and the shape and distribution of M/A were the main factors affecting the fracture toughness of this region. High-angle grain boundaries also formed a significant barrier to crack propagation. The coarse M/A constituents and long rod-shaped M/A could easily serve as crack initiation or crack propagation paths.
- By studying the relationship between the position of the hot zone and toughness, we found that the brittle

valley of the heat-affected zone accounted for about 50% of its width. Therefore, improving the toughness of the brittle valley zone is the main objective for enhancing the impact toughness of the weld, especially by optimizing the content, morphology, and distribution of the M/A constituents in the ICHAZ and SCHAZ.

Acknowledgements The authors appreciate the financial support from National Key Research and Development Program of China (2017YFBO304900).

Declarations

Conflict of interest All authors disclosed no relevant relationships.

References

- X. Zhang, J. Wang, S. Liu, L. Yan, C. Song, H. Yu, *Mater. Sci. Eng. A* 861 (2022) 144355.
- L. Wang, S. Wang, *Materials* 16 (2023) 3578.
- L.Y. Sun, X. Liu, X. Xu, S.W. Lei, H.G. Li, Q.J. Zhai, *J. Iron Steel Res. Int.* 29 (2022) 1513–1525.
- O. Panchenko, I. Kladov, D. Kurushkin, L. Zhabrev, E. Ryl'kov, M. Zamozdra, *Mater. Sci. Eng. A* 851 (2022) 143569.
- X. Ye, S. Cui, T. Liu, Q. Ma, G. Liu, Z. Huang, J. Guo, S. Yin, *Coatings* 13 (2023) 706.
- G. Ma, Y. Chen, G. Wu, S. Wang, T. Li, W. Liu, H. Wu, J. Gao, H. Zhao, C. Zhang, X. Mao, *Crystals* 13 (2023) 714.
- Q. Chang, Y. Cao, Y. Zhen, G. Wu, F. Li, *Int. J. Pres. Ves. Pip.* 20 (2023) 104940.

- [8] Y. Wang, Z. Guo, X. Bai, C. Yuan, *Ocean Eng.* 235 (2021) 109385.
- [9] X. Wang, D. Wang, L. Dai, C. Deng, C. Li, Y. Wang, K. Shen, *Materials* 15 (2022) 6646.
- [10] G. Wang, J. Wang, L. Yin, H. Hu, Z. Yao, *Materials* 13 (2020) 121.
- [11] Y. Dong, D. Liu, L. Hong, J. Liu, X. Zuo, *Metals* 12 (2022) 716.
- [12] Y. Liu, R. Liu, B. Liu, Z. Zhu, Y. Li, H. Chen, *Mater. Charact.* 186 (2022) 111811.
- [13] J. Luo, S. Luo, L. Li, L. Zhang, G. Wu, L. Zhu, *Nat. Gas Ind. B* 6 (2019) 138–144.
- [14] X. Wang, D. Wang, C. Deng, C. Li, *Materials* 15 (2022) 4458.
- [15] Z. Gao, B. Gong, B. Wang, D. Wang, C. Deng, Y. Yu, *Int. J. Hydrogen Energy* 46 (2021) 38535–38550.
- [16] Z. Gu, X. Zhu, Q. Ding, S. Duan, P. Wang, X. Lu, *Eng. Fail. Anal.* 150 (2023) 107299.
- [17] M. Arandelović, S. Sedmak, R. Jovičić, A. Petrović, S. Dikić, *Procedia Struct. Integr.* 42 (2022) 985–991.
- [18] X. Qi, P. Huan, X. Wang, Z. Liu, X. Shen, Y. Gao, H. Di, *Mater. Today Commun.* 31 (2022) 103413.
- [19] J.M. Giarola, J.W. Calderón-Hernández, J.M. Quispe-Avilés, J.A. Avila, W.W. Bose Filho, *Int. J. Hydrogen Energy* 46 (2021) 28166–28179.
- [20] M. St. Węglowski, S. Dymek, M. Kopyściański, J. Niagaj, J. Rykała, W. De Waele, S. Hertelé, *Archiv. Civ. Mech. Eng.* 20 (2020) 14.
- [21] J. Jiang, Z.Y. Peng, M. Ye, Y.B. Wang, X. Wang, W. Bao, *J. Mater. Civ. Eng.* 33 (2021) 04021186.
- [22] M. Mahmoudiniya, A.H. Kokabi, M. Goodarzi, L.A.I. Kestens, *Mater. Sci. Eng. A* 769 (2020) 138490.
- [23] J. Du, J. Li, Y. Feng, J. Ning, S. Liu, F. Zhang, *Mater. Des.* 221 (2022) 110953.
- [24] K.S. Arora, S.R. Pandu, N. Shajan, P. Pathak, M. Shome, *Int. J. Pres. Ves. Pip.* 163 (2018) 36–44.
- [25] J.C.F. Jorge, L.F.G. de Souza, M.C. Mendes, I.S. Bott, L.S. Araújo, V.R. dos Santos, J.M.A. Rebello, G.M. Evans, *J. Mater. Res. Technol.* 10 (2021) 471–501.
- [26] X. Yang, X. Di, X. Liu, D. Wang, C. Li, *Mater. Charact.* 155 (2019) 109818.
- [27] M.F.G. Ramirez, J.W.C. Hernández, D.H. Ladino, M. Masoumi, H. Goldenstein, *J. Mater. Res. Technol.* 14 (2021) 1848–1861.
- [28] N. Huda, Y. Wang, L. Li, A.P. Gerlich, *Mater. Sci. Eng. A* 765 (2019) 138301.
- [29] K. Yin, F. Wei, J. Wang, H. Ma, P. Jin, *Mater. Today Commun.* 35 (2023) 106234.
- [30] R. Chen, Z. Li, Q. Zhang, X. Li, *Corros. Sci.* 209 (2022) 110784.
- [31] S. Chen, Q. Yu, *Scripta Mater.* 163 (2019) 148–151.
- [32] R. Song, D. Ponge, R. Kaspar, D. Raabe, *Int. J. Mater. Res.* 95 (2004) 513–517.
- [33] M. Glienke, M. Vaidya, K. Gururaj, L. Daum, B. Tas, L. Rogal, K.G. Pradeep, S.V. Divinski, G. Wilde, *Acta Mater.* 195 (2020) 304–316.
- [34] Y. Wang, X. Ma, G. Zhao, X. Xu, X. Chen, C. Zhang, *J. Mater. Sci. Technol.* 82 (2021) 161–178.
- [35] Q. Ren, Z. Kou, J. Wu, T. Hou, P. Xu, *Metals* 13 (2023) 771.
- [36] Y. Fan, G. Gao, X. Gui, B. Bai, Z. Yang, *Int. J. Fatigue* 173 (2023) 107706.
- [37] S.G. Lee, S.S. Sohn, B. Kim, W.G. Kim, K.K. Um, S. Lee, *Mater. Sci. Eng. A* 715 (2018) 332–339.
- [38] X. Wang, Z. Wang, Z. Xie, X. Ma, S. Subramanian, C. Shang, X. Li, *J. Wang, Math. Biosci. Eng.* 16 (2019) 7494–7509.
- [39] S.G. Lee, B. Kim, S.S. Sohn, W.G. Kim, K.K. Um, S. Lee, *Mater. Sci. Eng. A* 760 (2019) 125–133.
- [40] N. Huda, A. Midawi, J.A. Gianetto, A.P. Gerlich, *J. Mater. Res. Technol.* 12 (2021) 613–628.
- [41] Z. Liao, Y. Dong, Y. Du, X. Wang, M. Qi, H. Wu, X. Gao, L. Du, *J. Mater. Res. Technol.* 23 (2023) 1471–1486.

Springer Nature or its licensor (e.g. a society or other partner) holds exclusive rights to this article under a publishing agreement with the author(s) or other rightsholder(s); author self-archiving of the accepted manuscript version of this article is solely governed by the terms of such publishing agreement and applicable law.